ACS OMEGA

Article

Cite This: ACS Omega 2020, 5, 145−157

http://pubs.acs.org/journal/acsodf

Development of Rhodamine 6G-Based Fluorescent Chemosensors for Al^{3+}-Ion Detection: Effect of Ring Strain and Substituent in Enhancing Its Sensing Performance

Jayanta Mandal,[†] Pravat Ghorai,[†] Kunal Pal,[‡] Tanurima Bhaumik,[†] Parimal Karmakar,[‡] and Amrita Saha*[,†]

[†]Department of Chemistry and [‡]Department of Life Science and Biotechnology, Jadavpur University, Kolkata 700032, India

Supporting Information

ABSTRACT: Four rhodamine 6G-based chemosensors (H_3L1-H_3L4) are designed for selective detection of Al^{3+} ion. They are characterized using various spectroscopic techniques and X-ray crystallography. All absorption and emission spectral studies have been performed in 10 mM *N*-(2-hydroxyethyl)-piperazine-*N*′-ethanesulfonic acid (HEPES) buffer solution at pH 7.4 in H_2O/MeOH (9:1, v/v) at 25 °C. In absorption spectra, chemosensors exhibit an intense band around 530 nm in the presence of Al^{3+} ion. Chemosensors (H_3L1-H_3L4) are nonfluorescent when excited around 490 nm. The presence of Al^{3+} ion enhances the emission intensity (555 nm) many times. The formation of complexes **1**−**4** is established with the aid of different spectroscopic techniques. The limit of detection value obtained in the nanomolar range confirms the high sensitivity of the probes toward Al^{3+} ion. It has been observed that the presence of aliphatic spacers in the diamine part and different halogen substituents in the salicylaldehyde part strongly influences the selectivity of the chemosensors toward Al^{3+} ion. The propensity of the chemosensors to identify intracellular Al^{3+} ions in triple-negative human breast cancer cell line MDA-MB-468 by fluorescence imaging is also examined in this study.

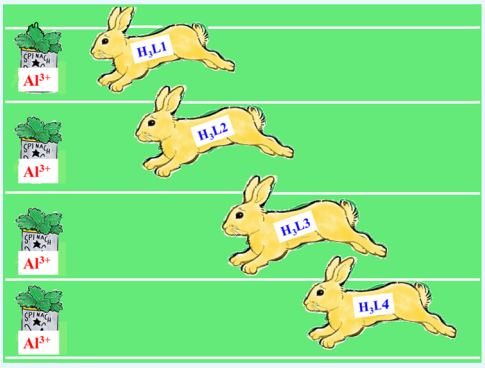

INTRODUCTION

Metal ions play a crucial role in human life and in the environment. Therefore, their detection is of immense importance to biologists, chemists, and environmentalists.[1] Scientists emerge in the development of new methodologies for recognition of these cations.[2−5] Design and synthesis of new chemosensors for the selective detection of biologically and environmentally important cations needs a special mention in this context.[6,7]

Aluminum is the highest abundant metal in the earth's crust.[8−10] Materials prepared from aluminum are widely used in our society. They are used in food additives, textile industry, water treatment plants, paper industry, production of light alloys, medicines (antacids), cookware, etc. Aluminum toxicity causes Alzheimer's and Parkinson's diseases.[11] Other Al-contaminated diseases are amyotrophic lateral sclerosis, microcytic hypochromic anemia, osteomalacia, and breast cancer.[12−17] Preparation of chemosensors for the selective detection of Al^{3+} ion is a challenging task owing to its weak coordination ability, strong hydration ability, and interferences from other trivalent ions like Cr^{3+} and Fe^{3+}. To date, a considerable number of organic probes for Al^{3+}ion[18−23] have been synthesized, most of which suffer from some drawbacks like insolubility in aqueous solution, synthetic procedures with multiple steps, poor sensitivity and selectivity with target metal ions, etc.[24−26] Al^{3+}-sensing organic probes consist of important fluorophoric units like rhodamine, anthraquinone, BODIPY, salicylaldehyde, fluorescein, coumarin, etc.[27−33] Rhodamine-based chemophores are colorless and nonfluorescent due to the presence of spirolactam ring. The sensing mechanism is basically opening of the spirolactam ring resulting in a strong emission. Low pH or acidic condition also initiates opening of the spirolactam ring. Therefore, selective choice of metal ion can initiate spirolactam ring opening of rhodamine-based probes. A literature study reveals that rhodamine-based probes can selectively detect various metal ions like Al^{3+}, Fe^{3+}, Cr^{3+}, Hg^{2+}, Cu^{2+}, etc.[34−43] Some recently reported rhodamine-based important chemosensors are collected in Chart S1 (Supporting Information). Chart S1 clearly shows that chemosensors reported in the present work have certain advantages regarding the crystal structure, real sample analysis, and cell imaging study in comparison to previously reported data.[44] Yang et al.[44a] reported two rhodamine-pyrazole-based both colorimetric and turn-on fluorescent chemosensors for dual detection of Ni^{2+} and Al^{3+} ions in alcohol and aqueous DMF medium. Jeong et al.[44b] synthesized rhodamine-chloronicotinaldehyde-based "OFF−ON" chemosensor for colorimetric and fluorimetric detection of Al^{3+} in acetonitrile medium. Chemate and

Received: July 15, 2019
Accepted: November 14, 2019
Published: December 27, 2019

DOI: 10.1021/acsomega.9b02181
ACS Omega 2020, 5, 145−157

Scheme 1. Route of Preparation of Chemosensors (H_3L1−H_3L4) and Complexes 1−4

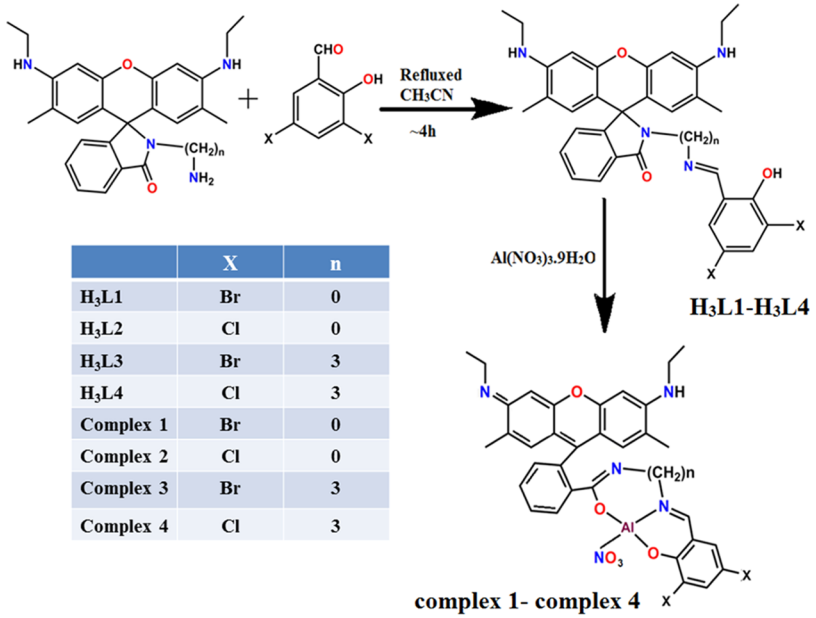

	X	n
H_3L1	Br	0
H_3L2	Cl	0
H_3L3	Br	3
H_3L4	Cl	3
Complex 1	Br	0
Complex 2	Cl	0
Complex 3	Br	3
Complex 4	Cl	3

co-workers have used two rhodamine-based OFF−ON fluorescent chemosensors for dual detection of Hg^{2+} and Al^{3+} in aqueous solution.[44c] Maity and co-workers prepared a rhodamine-1,2,3-triazole-based chemosensor for dual detection of Al^{3+} and fluoride or acetate ions in CH_3OH−H_2O (9:1) medium.[44d] The above examples did not report crystal structures of the chemosensors and their biological cell imaging studies. In this work, we have successfully elucidated crystal structures of all four chemosensors and also performed their biological studies. In an interesting work, Roy and co-workers synthesized a rhodamine-based dual chemosensor for detection of Al^{3+} and Zn^{2+} ions in *N*-(2-hydroxyethyl)-piperazine-*N*′-ethanesulfonic acid (HEPES) buffer.[44e] Ghosh and co-workers have prepared a chemosensor using the rhodamine unit for detection and discrimination of Al^{3+} and Hg^{2+} ions in HEPES buffer.[44f] Alam and co-workers synthesized a rhodamine-based trivalent fluorescent sensor which can selectively detect Fe^{3+}, Al^{3+}, and Cr^{3+} ions in CH_3OH−H_2O (1:1).[44g] These works clearly show that the chemosensors did not achieve their selectively toward Al^{3+} ions, whereas our synthesized chemosensors show selectivity only toward Al^{3+} ions. Fu and co-workers[44h] synthesized a rhodamine 6G-containing fluorescent probe for Al^{3+}ion. Sahana et al. reported a rhodamine−pyrene compound for selective colorimetric and fluorimetric detection of Al^{3+} ion and living cell imaging study.[44i] In the above chemosensors, the lmit of detection (LOD) values are observed in the micromolar range; interestingly, our reported chemosensors give LOD values in the nanomolar range. Roy et al. reported a rhodamine-based fluorescent chemosensor[44j] for selective detection of Al^{3+} ions in H_2O/MeOH = 1: 9 (v/v) medium. Sen and co-workers also reported a rhodamine-based Al^{3+}-ion-sensing organic compound[44k] in EtOH−water, 1: 3 (v/v) medium. Sahana and group synthesized a rhodamine-based fluorescent probe[44l] for selective detection of Al^{3+} ions in EtOH−water, 4: 1 (v/v) medium. In all of these examples, medium is mainly organoaqueous, whereas our Al^{3+}-ions-sensing studies are performed in MeOH−water, 1: 9 (v/v) medium.

In this work, we have chosen hydrazine and 1,3 diaminopropane as amines, 3,5-dichlorosalicylaldehyde and 3,5-dibromosalicylaldehyde as aldehydes to prepare four different rhodamine 6G-based chemosensors, **H_3L1**, **H_3L2**, **H_3L3**, and **H_3L4**, respectively. All of the four chemosensors selectively detect Al^{3+} both colorimetrically and fluorimetrically. The structure−property relationship is established in this work. Variation of amines and halogen substituents in the salicylaldehyde part controls the extent of selectivity toward Al^{3+} ion. A significant variation in different sensing parameters such as LOD, binding constant, and naked eye detection of Al^{3+} ion is observed during this study. These biocompatible chemosensors (**H_3L1**−**H_3L4**) also exhibit cell permeability and sense intracellular Al^{3+} ion present in breast cancer cell line, MDA-MB-468 cells.

RESULTS AND DISCUSSION

Synthesis and Characterization. *N*-(Rhodamine-6G)-lactam-hydrazine and *N*-(Rhodamine-6G)lactam-propylenediamine have been synthesized according to a published procedure.[45] The chemosensors (**H_3L1**−**H_3L4**) are synthesized by the Schiff base condensation reaction using rhodamine-6G-based amine and 3,5-dibromosalicylaldehyde or 3,5-dichlorosalicylaldehyde. They are carefully characterized using different spectroscopy techniques (UV−vis, Fourier transform infrared (FT-IR), and NMR), and the purity is verified with ESI-MS and C, H, N analysis (Figures S1−S5, Supporting Information).

H_3L1−**H_3L4** react with $Al(NO_3)_3{\cdot}9H_2O$ in a 1:1 ratio to produce complexes **1**−**4** (Scheme 1). They are characterized by ^{1}H NMR, ^{13}C NMR, FT-IR spectroscopy, C, H, N analysis, and electrospray ionization mass spectrometry (ESI-MS) analysis. The experimentally obtained ESI-MS data are well matched with their simulated result (Figures S6−S10, Supporting Information). Detail data are presented in Experimental Section.

Crystal Structure Descriptions of Chemosensors (H_3L1**−**H_3L4**).** We have successfully developed X-ray-quality crystals of **H_3L1**, **H_3L2**, and **H_3L3**, **H_3L4**, which are poorly

DOI: 10.1021/acsomega.9b02181
ACS Omega 2020, 5, 145−157

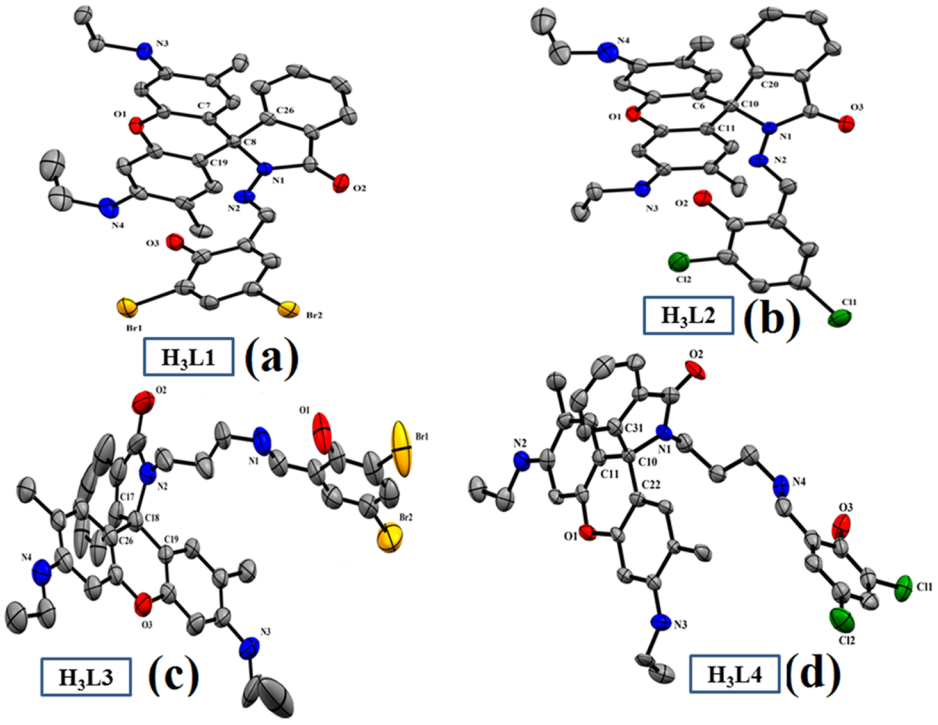

Figure 1. ORTEP view of the chemosensors (a) = H_3L1, (b) = H_3L2, (c) = H_3L3, and (d) = H_3L4. Atoms are shown as 30% thermal ellipsoids. Here, H atoms are omitted for clarity.

diffracted. H_3L1 and H_3L2 are formed with a triclinic crystal system with a $P\bar{1}$ space group, whereas H_3L3 and H_3L4 crystals are developed in the monoclinic system with a $P2_1/c$ space group (Table S1). ORTEP views of the chemosensors are shown in Figure 1 (H_3L1–H_3L4, respectively). Important bond distances and bond angles are collected in Tables S2 and S3, respectively (Supporting Information). The organic molecule is nonplanar, and it confirms the Schiff base condensation reaction along with the presence of a spirolactam ring and a xanthene unit within the molecule. The C−O and C−N bond distances of the chemosensors vary within the range of 1.217−1.381 and 1.274−1.441 Å, respectively.

NMR Studies. All of the chemosensors and Al^{3+}−probe complexes give well-resolved ^{1}H NMR spectra in DMSO-d_6 solvent. In H_3L1, the phenolic OH and imine proton appear as a sharp singlets at 11.56 and 8.90 ppm, respectively. Aromatic protons appear in the region 7.94−6.20 ppm. Aliphatic amine (−NH) protons appear as triplet at 5.11 ppm. Aliphatic CH_2 protons appear as quartet at 3.13 ppm. Aromatic CH_3 protons appear as singlet at 1.84 ppm, whereas aliphatic CH_3 protons appear as triplet at 1.20 ppm (Figures S11–S14, Supporting Information).

In complex **1**, the phenolic −OH peak disappears due to complexation and imine proton shifts to downfield and appears as a sharp singlet at 9.30 ppm. We also observe significant changes in the aromatic peak positions and broadening of the peaks due to complexation. During complexation, one NH proton of the aliphatic part disappears and the other appears as a broad peak at 5.11 ppm. Aliphatic CH_2 protons merged with water molecules and appear as multiplet at 3.50 ppm. Aromatic CH_3 protons appear as singlet at 1.87 ppm, and aliphatic CH_3 protons appear as triplet at 1.22 ppm (Figures S15–S18).

All of the chemosensors and probe-bound Al^{3+} complexes give clean ^{13}C NMR spectra in the DMSO-d_6 solvent. In H_3L1, spirolactam amide carbon appears at 165.58 and phenolic carbon appears at 164.21 ppm. Imine carbon appears at 161.87 ppm. Aromatic carbons are present in the region 151.88−96.32 ppm. The carbon atom connecting the xanthene part and the spirolactam ring is sp^3-hybridized and appears at 66.24 ppm. Aromatic CH_3 carbons appear with double intensity at 37.92 ppm. Aliphatic CH_2 and CH_3 carbons appear with double intensity at 17.44 and 14.59 ppm, respectively (Figures S19–S22, Supporting Information).

In complex **1**, spirolactam amide carbon appears at 167.58, phenolic carbon appears at 165.90 ppm, and imine carbon appears at 163.37 ppm. These three pecks are shifted to downfield due to metal coordination. Aromatic carbons appear within 151.88−96.32 ppm. Since metal coordination results spirolactam ring opening, the sp^3-hybridized carbon atom connecting the xanthene part and the spirolactam ring now becomes sp^2-hybridized and appears at 134.90 ppm. Aromatic CH_3 carbons appear with double intensity at 37.92 ppm. Aliphatic CH_2 and CH_3 carbons appear with double intensity at 17.44 and 14.59 ppm, respectively (Figures S23–S26, Supporting Information).

Absorption Spectral Analysis. The UV−vis spectra of chemosensors (H_3L1–H_3L4) are first examined in 10 mM HEPES buffer solution at pH 7.4 (9:1, water/methanol, v/v). Chemosensors H_3L1 and H_3L2 exhibit well-resolved bands at ∼290 and ∼345 nm, whereas H_3L3 and H_3L4 show a well-defined band at ∼420 nm. Peaks are represented as $\pi \rightarrow \pi^*$ and $n \rightarrow \pi^*$ type of transitions. Interestingly, upon successive addition of Al^{3+} ions (0−11 μM, 10 mM HEPES buffer solution; pH 7.4; 9:1, water/methanol, v/v) to the chemosensor (10 μM), a new peak appears at ∼530 nm with significant changes in the spectra of all chemosensors (H_3L1–H_3L4). In H_3L1 and H_3L2, absorbance of peaks at ∼290 and ∼345 nm gradually increase, whereas in H_3L3 and H_3L4, the absorbance of peak at ∼420 nm gradually decreases (Figures 2 and S27–S29, Supporting Information). In the presence of

DOI: 10.1021/acsomega.9b02181
ACS Omega 2020, 5, 145−157

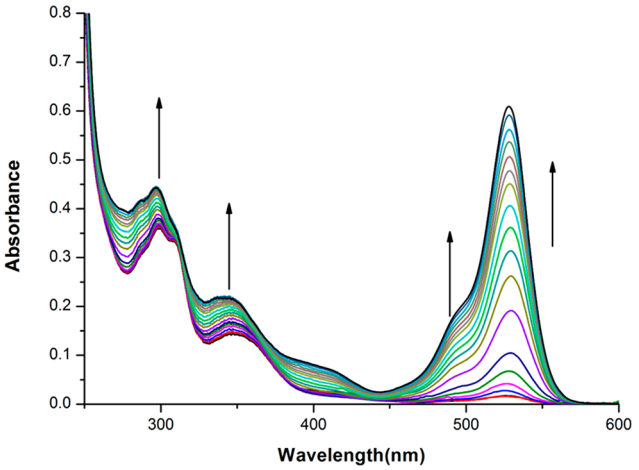

Figure 2. Absorption titration study of H_3L1 (10 μM) with gradual addition of Al^{3+}, 0−11 μM in 10 mM HEPES buffer at pH 7.4.

Al^{3+}, spirolactam ring opening occurs, followed by the coordination of the cation. Here, the Al^{3+} ion binds with phenoxido oxygen, imine nitrogen, and amide oxygen of the chemosensor. Spirolactam ring opening results reorientation of protons within the aromatic ring and consequently removal of one primary amine proton. Generation of a new peak at ∼530 nm in the presence of Al^{3+} ions also confirms structural rearrangement within the organic molecule. The color of the solution turns fluorescent pinkish yellow. Saturation has been observed in the presence of 1.1 equiv of Al^{3+} ions to the chemosensor. The 1:1 binding stoichiometry of the chemosensors with Al^{3+} ions has been confirmed by Job's plot analysis (Figures S30−S33, Supporting Information). These results have been further supported by ESI-MS analysis. It is important to mention that the addition of different cations (Cd^{2+}, Hg^{2+}, Pb^{2+}, Zn^{2+}, Ag^{+}, Mn^{2+}, Fe^{3+}, Co^{2+}, Ni^{2+}, Na^{+}, K^{+}, Mg^{2+}, and Ca^{2+}) did not change the initial absorption spectrum of the chemosensor appreciably.

Fluorescence Properties Analysis. The experiment is performed in 10 mM HEPES buffer at pH = 7.4 (9:1, water/methanol, v/v) at ambient conditions. When excited at 345 nm, probes (10 μM) are nonfluorescent. Upon successive addition of Al^{3+} ions (0−11 μM) to the probe, an enormous fluorescence enhancement is observed at 555 nm (Figures 3 and S34−S36, Supporting Information). The fluorescence enhancement has a steady growth and finally reaches a maximum at 1.1 equiv of Al^{3+} ions. In fact, metal ions initiate opening of spirolactam ring followed by a long conjugation of π-electronic system within the probe (Figure S37). Generation of a fluorescence peak at 555 nm in the presence of Al^{3+} ions also proves the above fact. Interestingly, the values of increment in emission spectra is not equal for all of the probes. In the case of H_3L1 and H_3L2, the emission enhancement is 780- and 725-fold, whereas for H_3L3 and H_3L4, the enhancement is 425- and 391-fold.

The binding ability of the chemosensors toward Al^{3+} ions has been calculated using the Benesi−Hildebrand equation (eq 1) involving fluorescence titration curve[46]

$$1/(F - F_0) = 1/(F_{max} - F_0) + (1/K[C])\{1/(F_{max} - F_0)\} \quad (1)$$

here, F_{max}, F_0, and F_x are fluorescence intensities of chemosensors (H_3L1−H_3L4), in the presence of metal ions at saturation, free chemosensors (H_3L1−H_3L4), and any intermediate metal-ions concentration, respectively. K is denoted as the binding constant of the complexes, and the concentration of Al^{3+} ions is represented by C. The value of binding constant (K) of the complexes has been determined using the relation K = 1/slope. The binding constant values are 8.00 × 10^5, 6.90 × 10^5, 1.37 × 10^4, and 1.03 × 10^4 M^{-1}, respectively, for the chemosensors H_3L1−H_3L4 toward Al^{3+} ions (Figures S38−S41, Supporting Information). We have also performed fluorescence titrations of the chemosensors in the presence of Al^{3+} ions in aprotic solvent such as tetrahydrofuran (THF) to determine the binding constant in THF and to compare the difference of binding constant values determined in protic and aprotic solvents. The calculated binding constant values in THF are close to the previously calculated values measured in the HEPES buffer solution (9:1, water/methanol, v/v) (Table S4, Figures S38−S45, Supporting Information). Therefore, we can conclude that free chemosensors H_3L1−H_3L4 do not undergo deprotonation in solution (protic or aprotic). Al^{3+} ions can promote deprotonation of H_3L1−H_3L4 in both aqueous or nonaqueous solution.

The high selectivity of the chemosensors toward Al^{3+} ions is again established by competition assay experiment. Here, in the presence of chemosensor and Al^{3+} ions (1.0 equiv), different metal ions (Cd^{2+}, Hg^{2+}, Pb^{2+}, Zn^{2+}, Ag^{+}, Mn^{2+}, Fe^{3+}, Co^{2+}, Ni^{2+}, Na^{+}, K^{+}, Mg^{2+}, and Ca^{2+}) (Figures S46−S49, Supporting Information) and common anions ($S_2O_3^{2-}$, S^{2-}, SO_3^{2-}, HSO_4^{-}, SO_4^{2-}, SCN^{-}, N_3^{-}, OCN^{-}, AsO_4^{3-}, $H_2PO_4^{-}$, HPO_4^{2-}, PO_4^{3-}, ClO_4^{-}, AcO^{-}, NO_3^{-}, F^{-}, Cl^{-},PF_6^{-}, and

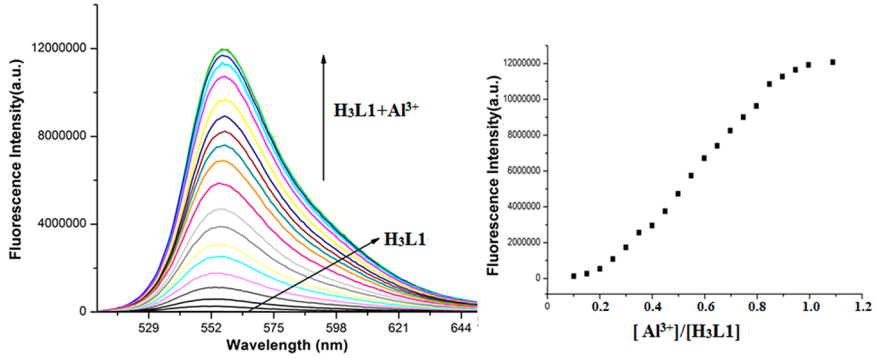

Figure 3. Fluorescence titration of H_3L1 (10 μM) in 10 mM HEPES buffer at pH = 7.4 by successive addition of Al^{3+} (0−11 μM) with λ_{em} = 555 nm (1/1 slit).

DOI: 10.1021/acsomega.9b02181
ACS Omega 2020, 5, 145−157

$P_2O_7^{4-}$) are added in excess amount (4.0 equiv) in 10 mM HEPES buffer solution at pH 7.4. Competition assay experiments clearly express high-fluorescent recognition of chemosensors ($\mathbf{H_3L1}$−$\mathbf{H_3L4}$) for Al^{3+} ions over most of the metal ions and all common anions. It is important to mention that in the presence of Cr^{3+}, Mg^{2+}, Cu^{2+}, and Fe^{3+} ions little quenching in fluorescence intensity has been observed (Figures 4 and S50−S56, Supporting Information).

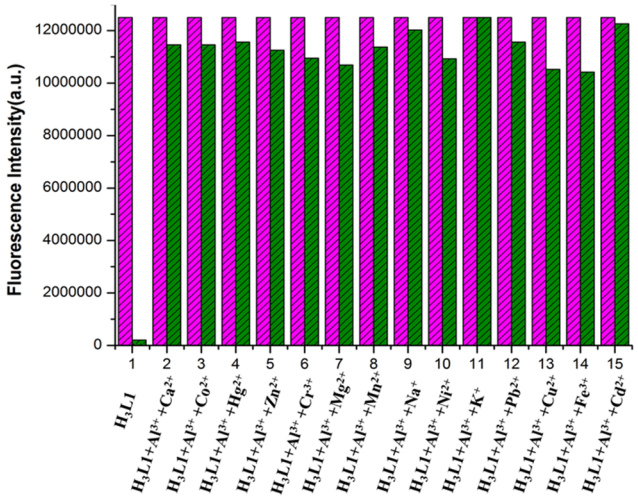

Figure 4. Relative fluorescence intensity diagram of [$\mathbf{H_3L1}$-Al^{3+}] system in the presence of different cations in 10 mM HEPES buffer at pH 7.4. 1 = only $\mathbf{H_3L1}$ and (2−15) = $\mathbf{H_3L1}$ (10 μM) + Al^{3+} (10 μM) + M^{n+} (40 μM), where M^{n+} = (2—Ca^{2+}, 3—Co^{2+}, 4—Hg^{2+}, 5—Zn^{2+}, 6—Cr^{3+}, 7—Mg^{2+}, 8—Mn^{2+}, 9—Na^{+}, 10—Ni^{2+}, 11—K^{+}, 12—Pb^{2+}, 13—Cu^{2+}, 14—Fe^{3+}, 15—Cd^{2+}).

Interestingly, all of the chemosensors, $\mathbf{H_3L1}$−$\mathbf{H_3L4}$, also act as colorimetric probe for selective detection of Al^{3+} ions. In the presence of Al^{3+} ions, all of the probes exhibit fluorescent pinkish yellow coloration, whereas they are almost colorless in the presence of common ions. The intensity of the Al^{3+} chemosensor increases in the order $\mathbf{H_3L1}$ > $\mathbf{H_3L2}$ > $\mathbf{H_3L3}$ > $\mathbf{H_3L4}$. Thus, the chemosensors will be a good choice for selective colorimetric detection of Al^{3+} ions in both environmental and biological fields (Figures 5 and S57−S59, Supporting Information). We have used saloon waste water and our laboratory tap water for real sample analysis. Al^{3+} ions present in saloon waste water and laboratory tap water are successfully detected by our chemosensors through the naked eye and under UV lamp (Figure S60, Supporting Information).

Reversibility and regeneration are two important factors for real-time application of the chemosensor. This is tested with the aid of sodium salt of ethylenediaminetetraacetic acid (Na_2EDTA) solution. The fluorescent pinkish yellow color of the probe−Al^{3+} complex disappears after addition of 1 equiv of Na_2EDTA with a simultaneous decrease in fluorescence intensity, which clearly indicates the regeneration of the free chemosensor. Again, addition of Al^{3+} ions to the probe gives back fluorescent pinkish yellow coloration. The whole cycle is repeated for at least five times to establish reversibility and regeneration point (Figure S61, Supporting Information).

Limit of detection (LOD) of the chemosensors toward Al^{3+} ions is estimated using the 3σ method.[47] The detection limits of the chemosensors ($\mathbf{H_3L1}$−$\mathbf{H_3L4}$) for the Al^{3+} ions are 1.4 × 10^{-9}, 2.50 × 10^{-9}, 0.40 × 10^{-8}, and 0.53 × 10^{-8} M, respectively.

The effect of pH on chemosensors ($\mathbf{H_3L1}$−$\mathbf{H_3L4}$) both in free condition and in the presence of Al^{3+} ions is studied fluorimetrically. It is well known that in acidic condition, the spirolactam ring of the chemosensor opens. A similar observation is also noticed in the presence of Al^{3+} ions. Therefore, both free chemosensor and chemosensor −Al^{3+} adduct will exhibit high fluorescence intensity at pH 2−4. At pH 5, a sharp decrease in the fluorescence intensity of free chemosensor is observed. After pH 5−11, its fluorescence intensity is very weak and remains unchanged. This observation suggests reconstruction of spirolactam ring in neutral and basic conditions. In the presence of Al^{3+} ions, the fluorescence intensity of the chemosensor decreases slightly at pH 4 and then it maintains a constant value up to pH 8. At pH 9, a sharp decrease in fluorescence intensity of chemosensor is observed. After pH 9−11, a very weak fluorescence intensity is observed. This is probably due to the generation of $Al(OH)_3$ and free chemosensor at higher pH. Rest of the probes ($\mathbf{H_3L2}$−$\mathbf{H_3L4}$) and probe−Al^{3+} adducts also followed a similar trend in fluorescence intensity at different pH values (Figures 6 and S62−S64, Supporting Information). The pH experiments

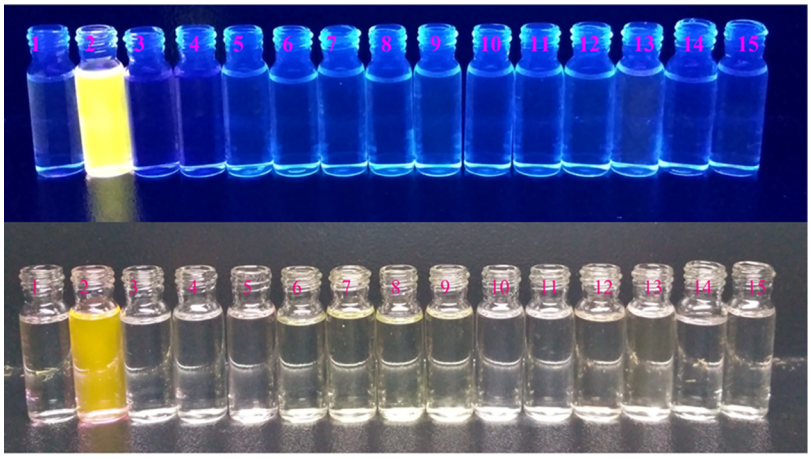

Figure 5. Visual color changes of chemosensor $\mathbf{H_3L1}$ (10 μM) in the presence of common metal ions (1 equiv) in 10 mM HEPES buffer (pH 7.4). The images in the bottom row and top row were taken under visible light and UV light, respectively, where 1 = only $\mathbf{H_3L1}$, 2−15 = $\mathbf{H_3L1}$ + different metal ions (Al^{3+}, Cu^{2+}, Cd^{2+}, Pb^{2+}, Hg^{2+}, Mn^{2+}, Fe^{3+}, Co^{2+}, Ni^{2+}, K^{+}, Na^{+}, Mg^{2+}, Ca^{2+}, and Zn^{2+}, respectively).

DOI: 10.1021/acsomega.9b02181
ACS Omega 2020, 5, 145−157

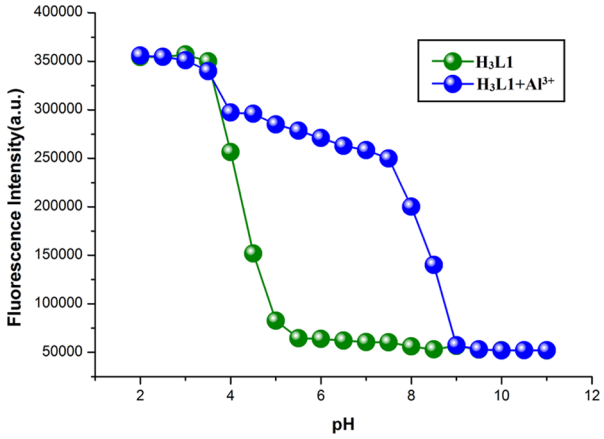

Figure 6. Fluorescence intensity of H_3L1 (10 μM) in the absence and presence of Al^{3+} ions (10 μM) at different pH values in 10 mM HEPES buffer.

show that these chemosensors can act as a selective fluorescent probe to recognize Al^{3+} ions in the presence of other metal ions in a biological system under physiological condition.

Lifetime and Quantum Yield Study. Lifetime measurements for the chemosensors (H_3L1–H_3L4) and complexes **1**–**4** are studied at 25 °C in 10 mM HEPES buffer (pH = 7.4) medium. The average values of fluorescence decay lifetime of the chemosensors and complexes **1**–**4** have been measured using the given formula ($\tau_f = a_1\tau_1 + a_2\tau_2$, where a_1 and a_2 are the relative amplitudes of the decay process). The average values of fluorescence lifetime of the chemosensors (**H3L1**–**H3L4**) and complexes **1**–**4** are 3.95, 2.56, 1.58, 1.06 ns and 6.8, 4.58, 4.53, 4.38 ns, respectively (Figures S69–S72 and Table S5, Supporting Information).

The fluorescence quantum yield (Φ) has been calculated as follows

$$\Phi_{sample} = \{(OD_{standard} \times A_{sample} \times \eta^2_{sample}) / (OD_{sample} \times A_{standard} \times \eta^2_{standard})\} \times \Phi_{standard} \quad (2)$$

In the above equation (eq 2), A is the area under the emission spectral curve, OD is the optical density of the compound at the excitation wavelength, and η is the refractive index of the solvent. The $\Phi_{standard}$ value is taken as 0.52 (for quinine sulfate).

The values of Φ for H_3L1–H_3L4 and probe–Al^{3+} complexes **1**–**4** are estimated to be 0.004, 0.003, 0.002, 0.004 and 0.24, 0.18, 0.13, 0.11, respectively (Table S5).

Mechanism of Fluorescence Intensity Enhancement in Chemosensors in the Order H_3L1 > H_3L2 > H_3L3 > H_3L4 in the Presence of Al^{3+} Ions. In this work, the sensing behavior of four rhodamine 6G-based chemosensors toward Al^{3+} ions is explored. The fluorescence intensity of the chemosensors increases abruptly in the presence of Al^{3+} ions due to opening of the spirolactam ring (Scheme 1). This mechanistic process has been supported by spectroscopic techniques such as ^1H, ^{13}C NMR, and FT-IR spectroscopy.[31,34,36−38,40] In the presence of Al^{3+} ions, appreciable changes are observed in their ^1H NMR spectrum of free chemosensors. The presence of Al^{3+} ion initiates spirolactam ring opening followed by rearrangement of double bonds. This results in the disappearance of one aliphatic amine (−NH) proton. The disappearance of phenolic −OH peak and downfield shift of imine proton (9.30 ppm) establishes coordination of phenoxido oxygen and imine nitrogen atom with the metal center. Changes in the spectral pattern of both aromatic and aliphatic protons are also observed after addition of Al^{3+}. In free chemosensor, the carbon atom connecting the xanthene part and the spirolactam ring is sp^3-hybridized, and it appears at 66.24 ppm. Interestingly, during metal coordination, spirolactam ring opens, and as a result, the sp^3-hybridized carbon atom becomes sp^2-hybridized and appears at 134.90 ppm (Figures S23–S26). Free chemosensors exhibit FT-IR stretching frequency of amide "C═O" bond and imine bond at ∼1699 and ∼1674 cm^{-1}, respectively, which are shifted significantly to lower values and appear at ∼1663 and ∼1646 cm^{-1}, respectively, after complexation. The sharp −OH peak at 3408 cm^{-1} also disappears after complexation. This observation suggests Al^{3+}-ion coordination with phenoxido oxygen, amide oxygen, and imine nitrogen of the chemosensor. Therefore, FT-IR data also supports spirolactam ring opening in the presence of Al^{3+} ion.

All chemosensors are colorless and nonfluorescent in visible light. The presence of Al^{3+} ions initiates opening of the spirolactam ring and the color becomes intense, pinkish yellow. The intensity of color is not similar. In the presence of Al^{3+} ions, the intensity increases in the order H_3L1 > H_3L2 > H_3L3 > H_3L4. Again, H_3L1, H_3L2, H_3L3, and H_3L4 exhibit around 780, 725, 425, and 391 times increase of fluorescence intensity in the presence of Al^{3+} ions, respectively. The LOD values are 1.4×10^{-9}, 2.50×10^{-9}, 0.40×10^{-8}, and 0.53×10^{-8} M, respectively. The values of binding constant of the probes toward Al^{3+} ions are 8.00×10^5, 6.90×10^5, 1.37×10^4, and 1.03×10^4 M^{-1}, respectively. Here, enhancement in the fluorescence intensity of the chemosensors in the presence of Al^{3+} ions and binding constant values of the probes toward Al^{3+} ions follow the same order H_3L1 > H_3L2 > H_3L3 > H_3L4. All these facts can be well explained by considering two factors: influence of ring strain during interaction between chemosensors and Al^{3+} ions and electron-withdrawing effect (−I effect) of the halogen substituent present in the chemosensors. Interestingly, the first effect is more pronounced. H_3L1 and H_3L2 form more stable five-membered chelate rings with Al^{3+} ions, whereas H_3L3 and H_3L4 form eight-membered chelate rings in the presence of Al^{3+} ions (Figure S37). Also, in the presence of a bromo substituent, the coordination ability of the imine nitrogen and phenoxido oxygen of the respective chemosensor is relatively high in comparison with a chloro substituent due to the −I effect. Therefore, due to the formation of the most stable H_3L1–Al^{3+} complex, the intensity of the complex solution under visible light is maximum, binding constant is the highest and LOD value is the lowest among four chemosensors.

Biocompatibility Study of the Ligands. The cellular toxicities of the ligands (H_3L1, H_3L2, H_3L3, and H_3L4) are envisaged to determine the compatibility against the normal human lung fibroblast cells, WI-38. The cells are exposed with various concentrations (20–100 μM/mL) of the ligands. Then, the cells are incubated for 24 h and the cellular survivability is determined with the help of the MTT assay. From the results, no significant toxicity is observed even at enhanced concentrations of 100 μM (as seen in Figure S69, Supporting Information). Hence, the results clearly depict the biocompatibility of the ligands and also suggest that these

DOI: 10.1021/acsomega.9b02181
ACS Omega 2020, 5, 145−157

ligands have the potential to emerge as promising tools for application in biomedical fields.

Cell Imaging. The cellular internalization of the chemosensors (H_3L1-H_3L4) (10 μM) and Al^{3+}salt (10 μM) has been determined with the aid of detailed fluorescence microscopy studies. The fluorescence microscopy images reveal the presence of a promiscuous red fluorescent signal in the microscope (Figure 7). Henceforth, the results suggest

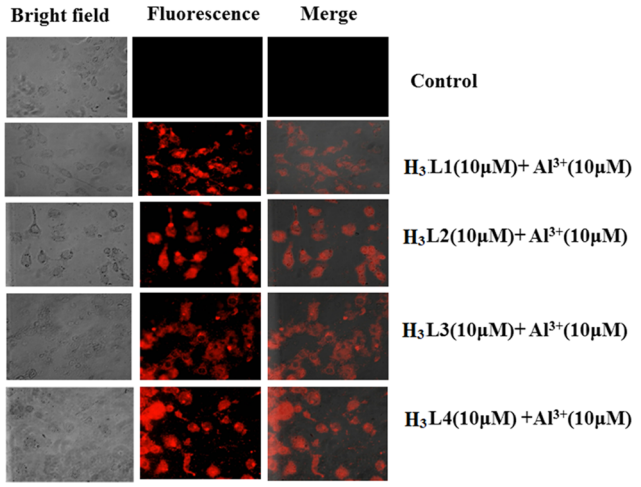

Figure 7. Bright-field, fluorescence, and merged microscopy images of untreated MDA-MB-468 (control) cells in the presence of chemosensor (H_3L1-H_3L4) (10 μM) + Al^{3+} (10 μM).

that the ligands and the Al^{3+} salts are promptly internalized by the cells, which in turn are responsible for the emergence of red fluorescent signal.

Density Functional Theory (DFT) Study. DFT and time-dependent DFT (TDDFT) studies are performed to establish the structural and electronic parameters of probes. Furthermore, to understand the nature, origin, and contribution of M.O.s for electronic transitions, a TDDFT study was performed. This study gives an idea of the quantity of energy associated with every individual transition. In each individual M.O., the contribution from both chemosensor and metal center has been computed. Therefore, DFT and TDDFT analyses play an important role to support and understand structural and electronic parameters of complexes.

Here, the geometry optimization of the chemosensors (H_3L1-H_3L4) has been performed using the DFT/B3LYP process. Some important bond distances and bond angles of all of the chemosensors (H_3L1-H_3L4) are listed in Tables S2 and S3. Energies (eV) of some selected M.O.s are included in Table S6. Contour plots of some selected molecular orbital of the chemosensors are depicted in Figure S70. Theoretical calculations reveal that in H_3L1, electron density in lowest unoccupied molecular orbital (LUMO) is mainly distributed over the xanthene part and electron density in highest occupied molecular orbital (HOMO) is mainly distributed over the xanthene part and spirolactam ring. In H_3L2, the electron density in LUMO is mainly distributed over the salicyl part and the spirolactam ring adjacent aromatic moiety and the electron density in HOMO is mainly distributed over the xanthene part. LUMOs of both H_3L3 and H_3L4 are mainly salicyl part-based, whereas HOMOs are mainly xanthene moiety-based.

TDDFT Study. Electronic transitions in chemosensors (H_3L1-H_3L4) are theoretically studied using the TDDFT, B3LYP/CPCM method. Important electronic transitions are given in Table S7. In theoretical calculations, for H_3L1 and H_3L2, intense absorption bands are found at around 355 and 345 nm, respectively. Major transitions for H_3L1 are HOMO − 2 → LUMO (88%) and HOMO − 1 → LUMO (74%) (Figure 8), whereas for H_3L2, the key transitions are HOMO

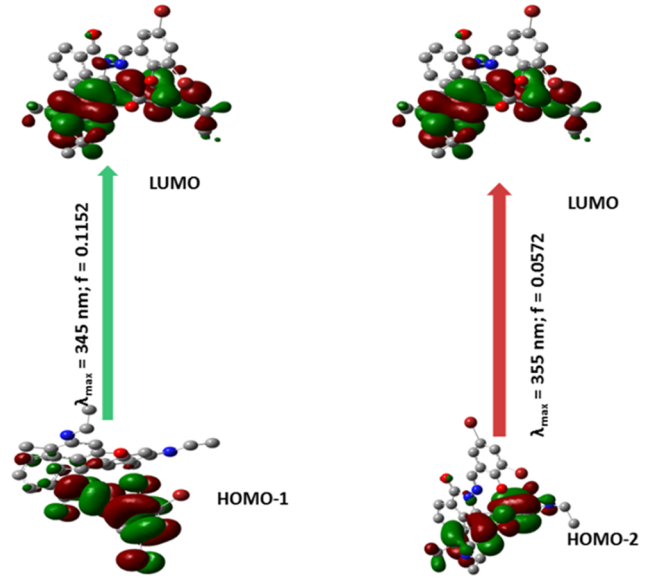

Figure 8. Pictorial representation of key transitions involved in UV−vis absorption of chemosensor H_3L1.

− 2 → LUMO (99%) and HOMO − 3 → LUMO (96%), respectively (Figure S71). In the case of H_3L3 and H_3L4, two major bands are observed at around 420 and 400 nm, which correspond to the HOMO → LUMO (96%) and HOMO − 1 → LUMO (95%) (H_3L3) (Figure S72) and HOMO → LUMO (97%) and HOMO − 1 → LUMO (96%) (H_3L4) (Figure S73).

SUMMARY

We have successfully developed four new rhodamine 6G-based fluorescent and colorimetric chemosensors H_3L1-H_3L4 for a rapid and selective detection of Al^{3+} ions. For visualization by the naked eye, the intensity of the color of probe−Al^{3+} ions increases in the order **HL4**-Al^{3+} < $HL_3^-Al^{3+}$ < **HL2**-Al^{3+} < **HL1**-Al^{3+}. All four chemosensors form a 1:1 complex with Al^{3+} ions, which has been proved by fluorescence measurements, ESI-MS analysis, and NMR studies. In fluorescence competition assay experiments, the selectivity of the probes toward Al^{3+} ions is established. Moreover, the reversibility is also achieved by addition of Na_2EDTA solution. H_3L1, H_3L2, H_3L3, and H_3L4 exhibit around 780, 725, 425, and 391 times enhancement in fluorescence intensity in the presence of Al^{3+} ions. Al^{3+} is detected in the nanomolar scale, and the LOD values are 1.4×10^{-9}, 2.50×10^{-9}, 0.40×10^{-8}, and 0.53×10^{-8} M, respectively. All of the probes are suitable for real-time quantitative detection of Al^{3+} ions in the field of environmental samples and biological systems. The values of binding constant of the probes toward Al^{3+} ions are 8.00×10^5, 6.90×10^5, 1.37×10^4, and 1.03×10^4 M^{-1}, respectively. In this work, we have also established the influence of ring strain and electron-

DOI: 10.1021/acsomega.9b02181
ACS Omega 2020, 5, 145−157

withdrawing effect (−I effect) of the halogen substituents present in the chemosensors during interaction between chemosensors and Al^{3+} ions. Interestingly, the first effect is more pronounced compare to the other. The color intensity difference of the probes in the presence of Al^{3+} ions under visible light, different binding constants, quantum yields, and LOD values of the probes toward Al^{3+} ions can be well explained in the light of the above two factors. **H_3L1** and **H_3L2** form more stable five-membered chelate ring with Al^{3+} ions, whereas **H_3L3** and **H_3L4** form an eight-membered chelate ring in the presence of Al^{3+} ions (Figure S37). Also, in the presence of bromo substituent, the coordination ability of the imine nitrogen and phenoxido oxygen of the respective chemosensor is relatively high in comparison to chloro substituent due to less −I effect. We are also successful in revealing its practical application by performing cell imaging study of chemosensors (**H_3L1**−**H_3L4**) using MDA-MB-468 cells. Furthermore, the probes are applied to detect intracellular Al^{3+} ions in live cells with no significant cytotoxicity. We have compared different factors like elucidation of crystal structure of the chemosensors, solubility of chemosensors in the aqueous medium for biological and real sample analyses, selectivity of the chemosensors toward Al^{3+} ions, and the nanomolar range of LOD values between chemosensors reported in this work and previously reported results. Interestingly, our chemosensors have successfully covered all of the points mentioned above in comparison to previously reported results presented in Chart S1.

EXPERIMENTAL SECTION

Materials and Physical Measurements Description. All reagent- or analytical-grade chemicals and solvents were collected from commercial sources and used without further purification. Elemental analysis was carried out using a PerkinElmer 240C elemental analyzer. Infrared spectra (400−4000 cm^{-1}) were recorded using KBr pellets on a Nicolet Magna IR 750 series-II FT-IR spectrophotometer. Absorption spectral data were collected using a Cary 60 spectrophotometer (Agilent) with a 1 cm path length quartz cell. Electron spray ionization mass (ESI-MS positive) spectra were noted using a MICROMASS Q-TOF mass spectrometer. A Fluromax-4 spectrofluorimeter was used to collect emission spectral data at room temperature (298 K) in HEPES buffer at pH = 7.4 solution under degassed condition. A time-resolved spectrofluorometer from IBH, U.K., was used to collect the fluorescence lifetime data, ^{1}H and ^{13}C NMR spectral data were collected using Bruker 400 and 300 spectrometers in DMSO-d_6 solvent.

X-ray Crystallography. Single-crystal X-ray data of chemosensors (**H_3L1**−**H_3L4**) were collected on a Bruker SMART APEX-II CCD diffractometer with the aid of graphite monochromated Mo Kα radiation (λ = 0.71073 Å) at room temperature. Data processing, structure solution, and refinement were examined using the Bruker Apex-II suite program. All available reflections data in the $2\theta_{max}$ range were harvested and corrected for Lorentz and polarization factors with Bruker SAINT plus.[48] Reflections were then corrected for absorption, interframe scaling, and different systematic errors with SADABS.[49] The structures were solved by the direct methods and refined with the help of a full-matrix least-squares technique based on F^2 with SHELX-2017/1 software package.[50] All of the nonhydrogen atoms were refined with anisotropic thermal parameters. C−H hydrogen atoms were attached at geometrical positions with U_{iso} = 1/2U_{eq} to those they are attached. Crystal data and details of data collection and refinement for **H_3L1**−**H_3L4** are collected in Table S1.

Synthesis of *N*-(Rhodamine-6G)lactam-hydrazine and *N*-(Rhodamine-6G)lactam-propylenediamine. *N*-(Rhodamine-6G)lactam-hydrazine and *N*-(Rhodamine-6G)lactam-propylenediamine were prepared by following the literature procedure.[45]

*Preparation of Chemosensor (**H_3L1**) [**H_3L1** = 2-((3,5-Dibromo-2-hydroxybenzylidene)amino)-3′,6′-bis-(ethylamino)-2′,7′-dimethylspiro[isoindoline-1,9′-xanthen]-3-one].* A mixture of *N*-(Rhodamine-6G)lactam-hydrazine (2.0 mmol, 0.8564 g) and 3,5-dichlorosalicylaldehyde (2.0 mmol, 0.5598 g) was heated in refluxing condition for ca. 4 h in acetonitrile solvent. Very light yellow crystals were collected after evaporation of the solvent.

Yield: 1.008 g (84%). Anal. calcd for $C_{33}H_{30}Br_2N_4O_3$: C 57.41%; H 4.38%; N 8.11%. Found: C 57.18%; H 4.30%; N 8.02%. IR (cm^{-1}, KBr): ν(C = N) 1621s; ν(O−H) 3408s; ν(C=O) 1663s (Figure S5). ESI-MS (positive) in MeOH: The molecular ion appeared at m/z = 691.11, consistent to [**H_3L1** + 1]$^+$ (Figure S1). UV−vis, λ_{max} (nm), (ε (dm^3 mol^{-1} cm^{-1})) in HEPES buffer at pH = 7.4: 345 (14020).

^{1}H NMR (400 MHz, DMSO-d_6) δ ppm: 1.20 (−CH_3) (t, 6H, J_1 = 7.2 Hz, J_2 = 6.8 Hz), 1.84 (Ar-CH_3) (s, 6H), 3.13 (−CH_2) (q, 4H), 5.11 (NH) (t, 2H, J_1 = 4.8 Hz J_2 = 5.2 Hz), 6.20 (Ar-CH) (s, 2H), 6.34 (Ar-CH) (s, 2H), 7.06 (Ar-CH) (d, 1H, J = 7.2 Hz), 7.53 (Ar-CH) (s, 1H), 7.56−7.72 (Ar-CH) (m, 2H), 7.94 (Ar-CH) (d, 1H, J = 7.2 Hz), 8.90 (−CH=N) (s, 1H), 11.56 (−OH) (s, 1H) (Figure S11).

^{13}C NMR (DMSO-d_6, 75 MHz) δ ppm: 14.59, 17.44, 37.92, 66.24, 96.32, 104.13, 106.13, 114.16, 119.04, 121.58, 123.78, 124.36, 127.20, 128.26, 129.47, 132.40, 134.90, 136.25, 148.47, 151.48, 151.88, 161.87, 164.27, 166.13 (Figure S19).

*Synthesis of Chemosensor (**H_3L2**) [**H_3L2** = 2-((3,5-Dichloro-2-hydroxybenzylidene)amino)-3′,6′-bis-(ethylamino)-2′,7′-dimethylspiro[isoindoline-1,9′-xanthen]-3-one].* A mixture of *N*-(Rhodamine-6G)lactam-hydrazine (2.0 mmol, 0.8564 g) and 3,5-dichlorosalicylaldehyde (2.0 mmol, 0.3820 g) was heated in refluxing condition for ca. 4 h in acetonitrile solvent. Very light yellow crystals were collected after evaporation of the solvent.

Yield: 1.200g (87%). Anal. calcd for $C_{33}H_{30}Cl_2N_4O_3$: C 65.89%; H 5.03%; N 9.31%. Found: C 65.68%; H 4.88%; N 9.29%. IR (cm^{-1}, KBr): ν(C=N) 1619s; ν(O−H) 3421s ν(C=O) 1699s (Figure S5). ESI-MS (positive) in MeOH: The base peak appeared at m/z = 623.18, corresponding to [**H_3L2** + 1]$^+$ (Figure S2). UV−vis, λ_{max} (nm), (ε (dm^3 mol^{-1} cm^{-1})) in HEPES buffer (10 mM) at pH = 7.4: 345 (20 440).

^{1}H NMR (400 MHz, DMSO-d_6) δ ppm: 1.20 (−CH_3) (t, 6H, J_1 = 7.2 Hz, J_2 = 6.8 Hz), 1.84 (Ar-CH_3) (s, 6H), 3.15−3.09 (−CH_2) (m, 4H), 5.11 (NH) (t, 2H, J = 5.2 Hz), 6.20 (Ar-CH) (s, 2H), 6.33 (Ar-CH) (s, 2H), 7.40 (Ar-CH) (s, 1H,), 7.51 (Ar-CH) (d, 1H, J = 7.2 Hz), 7.56−7.65 (Ar-CH) (m, 2H), 7.94 (Ar-CH) (d, 1H, J = 7.2 Hz), 8.96 (−CH=N) (s, 1H), 11.32 (−OH) (s, 1H) (Figure S12).

^{13}C NMR (DMSO-d_6, 75 MHz) δ ppm: 14.59, 17.44, 37.92, 66.24, 96.32, 104.13, 106.13, 114.13, 119.04, 121.58, 123.78, 124.36, 127.20, 128.26, 129.47, 132.40, 134.90, 136.25, 148.47, 151.48, 151.88, 154.27, 166.13 (Figure S20).

*Synthesis of Chemosensor (**H_3L3**) [**H_3L3** = 2-(3-((3,5-Dibromo-2-hydroxybenzylidene)amino)propyl)-3′,6′-bis-(ethylamino)-2′,7′-dimethylspiro[isoindoline-1,9′-xanthen]-*

DOI: 10.1021/acsomega.9b02181
ACS Omega 2020, 5, 145−157

3-one]. A mixture of *N*-(Rhodamine-6G)lactam-propylenediamine (2.0 mmol, 0.9128 g) and 3,5-dichlorosalicylaldehyde (2.0 mmol, 0.5598 g) was heated in refluxing condition for ca. 4 h in acetonitrile solvent. Yellow crystals were collected after evaporation of the solvent.

Yield: 1.171 g (80%). Anal. calcd for $C_{36}H_{36}Br_2N_4O_3$: C 59.03%; H 4.95%; N 7.65%. Found: C 58.88%; H 4.78%; N 9.29%. IR (cm^{-1}, KBr): ν(C═N) 1621s; ν(O−H) 3401s; ν(C═O) 1663s (Figure S5). ESI-MS (positive) in MeOH: The base peak appeared at m/z = 755.01, corresponding to $[\mathbf{H_3L3} + Na]^+$ (Figure S3). UV−vis, λ_{max} (nm), (ε (dm^3 mol^{-1} cm^{-1})) in HEPES buffer at pH = 7.4: 420 (47 570).

^{1}H NMR (400 MHz, DMSO-d_6) δ ppm: 1.20 (−CH_3) (t, 6H, J_1 = 9.6 Hz, J_2 = 9.2 Hz), 1.84 (Ar-CH_3) (s, 6H), 2.09 (−CH_2) (d, 2H, J = 16.8 Hz), 3.13 (−CH_2) (q, 4H), 5.11 (NH) (s, 2H), 6.20 (Ar-CH) (s, 2H), 6.34 (Ar-CH) (s, 2H), 7.06 (Ar-CH) (d, 1H, J = 9.2 Hz), 7.54 (Ar-CH) (s, 1H), 7.54−7.72 (Ar-CH) (m, 2H), 7.72 (Ar-CH) (s, 1H), 7.95 (Ar-CH) (d, 1H, J = 8.8 Hz), 8.90 (−CH═N) (s, 1H), 11.66 (−OH) (s, 1H) (Figure S13).

^{13}C NMR (DMSO-d_6, 75 MHz) δ ppm: 14.74, 16.74, 29.11, 37.54, 38.92, 54.60, 65.10, 96.64, 106.06, 107.72, 113.74, 118.00, 118.97, 122.76, 123.89, 128.17, 128.37, 131.16, 132.60, 132.81, 137.90, 147.54, 151.79, 153.42, 160.96, 163.82, 168.52 (Figure S21).

*Synthesis of Chemosensor (**H_3L4**) [**H_3L4** = 2-(3-((3,5-Dichloro-2-hydroxybenzylidene)amino)propyl)-3′,6′-bis-(ethylamino)-2′,7′-dimethylspiro[isoindoline-1,9′-xanthen]-3-one].* A mixture of *N*-(Rhodamine-6G)lactam-propylenediamine (2.0 mmol, 0.9128 g) and 3,5-dichlorosalicylaldehyde (2.0 mmol, 0.3820 g) was heated in refluxing condition for ca. 4 h in acetonitrile solvent. Yellow crystals were obtained after evaporation of the solvent.

Yield: 1.008 g (84%). Anal. calcd for $C_{36}H_{36}C_{l2}N_4O_3$: C 67.18%; H 5.64%; N 8.71%. Found: C 67.18%; H 5.58%; N 8.59%. IR (cm^{-1}, KBr): ν(C═N) 1634s; ν(O−H) 3430s; ν(C═O) 1674s (Figure S5). ESI-MS (positive) in MeOH: The base peak appeared at m/z = 665.13, corresponding to $[\mathbf{H_3L4} + Na]^+$ (Figure S4). UV−vis, λ_{max} (nm), (ε (dm^3 mol^{-1} cm^{-1})) in HEPES buffer (10 mM) at pH = 7.4: 420 (47 570).

^{1}H NMR (400 MHz, DMSO-d_6) δ ppm: 1.20 (−CH_3) (t, 6H, J_1 = 9.6 Hz, J_2 = 9.2 Hz), 1.84 (Ar-CH_3) (s, 6H), 2.09 (−CH_2) (d, 2H, J = 16.8 Hz), 3.14 (−CH_2) (q, 4H), 5.118 (NH) (s, 2H), 6.21 (Ar-CH) (s, 2H), 6.34 (Ar-CH) (s, 2H), 7.06 (Ar-CH) (d, 1H, J = 9.2 Hz), 7.54 (Ar-CH) (s, 1H), 7.54−7.72 (Ar-CH) (m, 2H), 7.72 (Ar-CH) (s, 1H), 7.94 (Ar-CH) (d, 1H J = 14.4 Hz), 8.92 (−CH═N) (s, 1H), 11.66 (−OH) (s, 1H) (Figure S14).

^{13}C NMR (DMSO-d_6, 75 MHz) δ ppm: 14.71, 16.72, 29.11, 37.54, 38.92, 54.60, 65.10, 96.65, 106.10, 117.99, 118.68, 121.13, 122.76, 123.61, 123.88, 128.15, 128.38, 128.99, 131.18, 132.57, 147.54, 151.79, 153.43, 159.18, 163.87, 168.49 (Figure S22).

*Synthesis of Complex (**1**) {[**Al(HL1)(NO_3)**] = N-(-3,5-Dibromo-2-oxidobenzylidene)-2-(-6-(ethylamino)-3-(ethylimino)-2,7-dimethyl-3H-xanthen-9-yl)-benzohydrazonatenitratoaluminium(III)}.* A 2 mL methanolic solution of aluminum nitrate nonahydrate (1.0 mmol, 0.375 g) was added carefully to a 20 mL acetonitrile solution of $\mathbf{H_3L1}$ (1.0 mmol, 0.690 g) followed by addition of triethylamine (1.0 mmol, ∼0.2 mL), and the resultant reaction mixture was stirred for ca. 3 h. A red solid mass was collected in high yield after slow evaporation of the solvent.

Yield: 0.512 g (78%). Anal. calcd for $C_{33}H_{28}AlBr_2N_5O_6$: C 50.99%; H 3.63%; N, 9.01%. Found: C 50.55%; H 3.51%; N 8.91%. IR (cm^{-1}, KBr): ν(C═N) 1601s; ν(NO_3^-) 1300s and 809s; ν(C═O) 1655s (Figure S10). ESI-MS (positive) in MeOH: The base peak was observed at m/z = 778.06, corresponding to $[\mathbf{Al(HL1)(NO_3)} + \mathbf{1}]^+$ (Figure S6). UV−vis, λ_{max} (nm), (ε (dm^3 mol^{-1} cm^{-1})) in HEPES buffer at pH = 7.4: 490 (27 500).

^{1}H NMR (400 MHz, DMSO-d_6) δ ppm: 1.22 (−CH_3) (t, 6H, J = 5.6 Hz), 1.87 (Ar-CH_3) (s, 6H), 3.50 (−CH_2) (t, 4H, J = 5.2 Hz), 5.11 (NH) (s, 1H), 6.10 (Ar-CH) (s, 2H), 6.27 (Ar-CH) (s, 2H), 6.97−6.95 (Ar-CH) (m, 2H), 7.52−7.50 (Ar-CH) (m, 2H), 7.61 (Ar-CH) (s, 1H), 7.81−7.80 (Ar-CH) (m, 2H), 9.30 (−CH═N) (s, 1H) (Figure S15).

^{13}C NMR (DMSO-d_6, 75 MHz) δ ppm: 14.59, 17.44, 37.92, 96.32, 104.13, 106.13, 114.16, 119.04, 121.58, 123.78, 124.36, 127.20, 128.26, 129.47, 132.40, 134.90, 136.25, 148.47, 151.48, 151.88, 163.37, 165.90, 167.58 (Figure S23).

*Synthesis of Complex (**2**) {[**Al(HL2)(NO_3)**] = N-(-3,5-Dichloro-2-oxidobenzylidene)-2-(-6-(ethylamino)-3-(ethylimino)-2,7-dimethyl-3H-xanthen-9-yl)-benzohydrazonatenitratoaluminium(III)}.* A 2 mL methanolic solution of aluminum nitrate nonahydrate (1.0 mmol, 0.375 g) was added carefully to a 20 mL acetonitrile solution of $\mathbf{H_3L2}$ (1.0 mmol, 0.690 g) followed by addition of triethylamine (1.0 mmol, ∼0.2 mL), and the resultant reaction mixture was stirred for ca. 3 h. A red solid mass was isolated in high yield after slow evaporation of the solvent.

Yield: 0.512 g (78%). Anal. calcd for $C_{33}H_{28}AlCl_2N_5O_6$: C 50.99%; H 3.63%; N 9.01%. Found: C 50.55%; H 3.51%; N 8.91% IR (cm^{-1}, KBr): ν(C═N) 1603s; ν(NO_3^-) 1300s and 810s; ν(C═O) 1646s (Figure S10). ESI-MS (positive) in MeOH: The base peak appeared at m/z = 696.22, corresponding to $[\mathbf{Al(HL2)(NO_3)} + \mathbf{Li}]^+$ (Figure S7). UV−vis, λ_{max} (nm), (ε (dm^3 mol^{-1} cm^{-1})) in HEPES buffer at pH = 7.4: 415 (19 670).

^{1}H NMR (400 MHz, DMSO-d_6) δ ppm: 1.22 (−CH_3) (t, 6H, J = 5.6 Hz), 1.87 (Ar-CH_3) (s, 6H), 3.50 (−CH_2) (t, 4H, J = 5.2 Hz), 5.12 (NH) (s, 1H), 6.12 (Ar-CH) (s, 2H), 6.28 (Ar-CH) (s, 2H), 6.97−6.95 (Ar-CH) (m, 2H), 7.52−7.50 (Ar-CH) (m, 2H), 7.61 (Ar-CH) (s, 1H), 7.82−7.80 (Ar-CH) (m, 2H), 9.33 (−CH═N) (s, 1H) (Figure S16).

^{13}C NMR (DMSO-d_6, 75 MHz) δ ppm: 14.59, 17.44, 37.92, 96.32, 105.10, 106.13, 114.13, 119.04, 121.58, 123.78, 124.36, 127.20, 128.26, 129.47, 132.40, 134.88, 136.25, 149.47, 152.48, 152.90, 162.87, 165.27, 169.13 (Figure S24).

*Synthesis of Complex (**3**) {[**Al(L3)(NO_3)**] = N-(3-((-3,5-Dibromo-2-oxidobenzylidene)amino)propyl)-2-(-6-(ethylamino)-3-(ethylimino)-2,7-dimethyl-3H-xanthen-9-yl)-benzimidatenitratoaluminium(III)}.* A 2 mL methanolic solution of aluminum nitrate nonahydrate (1.0 mmol, 0.375 g) was added carefully to a 20 mL acetonitrile solution of $\mathbf{H_3L3}$ (1.0 mmol, 0.690 g) followed by addition of triethylamine (1.0 mmol, ∼0.2 mL), and the resultant reaction mixture was stirred for ca. 3 h. A red solid mass was isolated in high yield after slow evaporation of the solvent.

Yield: 0.512 g (78%). Anal. calcd for $C_{36}H_{35}AlBr_2N_5O_6$: C 52.63%; H 4.42%; N 8.53%. Found: C 52.55%; H 4.31%; N 8.47%. IR (cm^{-1}, KBr): ν(C═N) 1630s; ν(NO_3^-) 1300s and 811s; ν(C═O) 773s (Figure S10). ESI-MS (positive) in MeOH: The base peak appeared at m/z = 822.09, corresponding to $[\mathbf{Al(HL3)(NO_3)} + \mathbf{1}]^+$ (Figure S8). UV−

DOI: 10.1021/acsomega.9b02181
ACS Omega 2020, 5, 145−157

vis, λ_{max} (nm), (ε (dm^3 mol^{-1} cm^{-1})) in HEPES buffer at pH = 7.4: 490 (28160).

^{1}H NMR (400 MHz, DMSO-d_6) δ ppm: 1.22 (−CH_3) (t, 6H, J = 5.6 Hz), 1.38 (−CH_2) (t, 2H, J_1 = 5.6 Hz, J_2 = 5.2 Hz), 1.87 (Ar-CH_3) (s, 6H), 2.62 (−CH_2) (d, 2H, J = 3.6 Hz), 3.05 (−CH_2) (t, 2H, J_1 = 4.2 Hz, J_2 = 4.5 Hz), 3.13 (−CH_2) (q, 4H), 5.11 (NH) (t, 1H), 6.01 (Ar-CH) (s, 2H), 6.20 (Ar-CH) (s, 2H), 6.97−6.96 (Ar-CH) (m, 2H), 7.52−7.50 (Ar-CH) (m, 2H), 7.61 (Ar-CH) (s, 1H), 7.82−7.80 (Ar-CH) (m, 2H), 9.32 (−CH═N) (s, 1H) (Figure S17).

^{13}C NMR (DMSO-d_6, 75 MHz) δ ppm: 14.74, 16.74,29.21, 37.54, 38.92, 54.80, 96.64, 106.06, 107.72, 113.74, 118.00, 118.97, 122.76, 123.89, 128.17, 128.37, 131.16, 132.60, 132.81, 137.90, 147.54, 151.79, 153.42, 160.96, 163.82, 168.52 (Figure S25).

*Synthesis of Complex (4) {[**Al(HL4)(NO$_3$)**] = N-(3-((-3,5-Dichloro-2-oxidobenzylidene)amino)propyl)-2-(-6-(ethylamino)-3-(ethylimino)-2,7-dimethyl-3H-xanthen-9-yl)-benzimidatenitratoaluminium(III)}.* A 2 mL methanolic solution of aluminum nitrate nonahydrate (1.0 mmol, 0.375 g) was added carefully to a 20 mL acetonitrile solution of **H_3L4** (1.0 mmol, 0.690 g) followed by addition of triethylamine (1.0 mmol, ∼0.2 mL), and the resultant reaction mixture was stirred for ca. 3 h. A red solid mass was isolated in high yield after slow evaporation of the solvent.

Yield: 0.512 g (78%). Anal. calcd for $C_{36}H_{35}AlCl_2N_5O_6$: C 59.02%; H 4.95%; N 9.56%. Found: C 58.85%; H 4.81%; N 9.21%. IR (cm^{-1}, KBr): ν(C═N) 1621s; ν(NO_3^-) 1310s and 813s; ν(C═O) 1634s (Figure S10). ESI-MS (positive) in MeOH: The base peak appeared at m/z = 732.16, corresponding to [**Al(HL4)(NO$_3$)** + **1**]$^+$ (Figure S9). UV−vis, λ_{max} (nm), (ε (dm^3 mol^{-1} cm^{-1})) in HEPES buffer at pH = 7.4: 490 (13 019).

^{1}H NMR (400 MHz, DMSO-d_6) δ ppm: 1.29 (−CH_3) (t, 6H J = 4.2 Hz), 1.38 (−CH_2) (t, 2H J_1 = 4.2 Hz, J_2 = 4.5 Hz), 1.87 (Ar-CH_3) (s, 6H), 2.62 (−CH_2) (d, 2H, J = 3.6 Hz), 3.05 (−CH_2) (t, 2H, J_1 = 4.2 Hz, J_2 = 4.5 Hz), 3.13 (−CH_2) (q, 4H), 5.11 (NH) (s, 1H), 6.10 (Ar-CH) (s, 2H), 6.27 (Ar-CH) (s, 2H), 6.97−6.94 (Ar-CH) (m, 2H), 7.52−7.50 (Ar-CH) (m, 2H), 7.61 (Ar-CH) (s, 1H), 7.87−7.85 (Ar-CH) (m, 2H), 9.35 (−CH═N) (s, 1H) (Figure S18).

^{13}C NMR (DMSO-d_6, 75 MHz) δ ppm: 14.71, 16.72, 29.11, 37.54, 54.60, 96.65, 106.10, 117.99, 118.68, 121.13, 122.76, 123.61, 123.88, 128.15, 128.38, 128.99, 131.88, 132.57, 147.74, 151.59, 153.73, 160.18, 164.57, 169.45 (Figure S26).

UV−Visible and Fluorescence Spectroscopy Experiment. Stock solutions of different ions (1×10^{-3} M) were prepared in a deionized water medium. A stock solution of the chemosensors (**H_3L1**−**H_3L4**) (1×10^{-3} M) was prepared in methanol medium. The chemosensors (**H_3L1**−**H_3L4**) solution was then diluted to 1×10^{-5} M as per requirement. A competitive assay of various cations and anions and other spectroscopic experiments were performed in aqueous methanolic HEPES buffer (10 mM) medium at pH 7.4. In the competitive assay experiments, the test samples were prepared by mixing appropriate amounts of the cations stock in 3 mL of chemosensors (**H_3L1**−**H_3L4**) solution (1×10^{-5} M).

Binding Stoichiometry (Job's Plot) Studies. Binding stoichiometry of the chemosensors with that of Al^{3+} ions is determined by Job's continuation method using absorption spectroscopy. At 25 °C, the absorbance was recorded for solutions where the concentrations of both chemosensor and Al^{3+} ions are varied but the sum of their concentrations was kept constant at 1×10^{-5} M, i.e., relative change in absorbance ($\Delta A/A_0$) against mole fraction of chemosensor. The break point in the resulting plot represents the mole fraction of chemosensor in the Al^{3+} complex. From the break point, the stoichiometry was determined. The final results reported were an average of at least three experiments.

Cell Culture. The triple-negative breast cancer cells of human origin, MDA-MB-468, are procured from the National Center for Cell Science (NCCS) Pune, India. The cells were cultured in an enriched cell culture medium, Dulbecco's modified Eagle's medium (DMEM), supplemented with 10% fetal bovine serum (FBS) and a mixture of appropriate antibiotics (streptomycin and penicillin at a dose of 100 units/mL). The cells were incubated at *a* temperature of 37 °C and in the prevalence of 5% CO_2.

Cell Visualization Studies. The human breast cancer cells, MDA-MB-468, were cultured on coverslips for a period of 24 h. Then, these cells were either left untreated or were exposed to *a* dose of ligands (10 μM) and Al^{3+} salt (10 μM). These treated cells were then incubated for 24 h at a temperature of 37 °C. Afterward, the cells were thoroughly washed with the help of 1 × PBS. Ultimately, the cells were envisaged with the help of a fluorescence microscope (Leica) following the mounting of the cells on a glass slide.

Computational Method. All computations were studied using the GAUSSIAN09 (G09)[51] software package. For optimization process, we used the density functional theory method at the B3LYP level,[52,53] and the standard 6-31+G(d) basis set for C, H, N, and O atoms[54,55] and the lanL2DZ effective potential (ECP) set of Hay and Wadt[56−58] for aluminum atoms have been selected for optimization.

TDDFT calculation was studied with the optimized geometry to ensure only positive eigen values. Time-dependent density functional theory (TDDFT)[59−61] was examined using conductor-like polarizable continuum model (CPCM)[62−64] and the same B3LYP level and basis sets in methanolic solvent system. GAUSSSUM[65] was utilized to calculate the fractional contributions of various groups to each molecular orbital.

■ ASSOCIATED CONTENT

Supporting Information

The Supporting Information is available free of charge at https://pubs.acs.org/doi/10.1021/acsomega.9b02181.

CCDC 1916757, 1916768, 1916759, and 1938716 include the supplementary crystallographic data for chemosensors (**H_3L1**−**H_3L4**), respectively (PDF)

H3L1 (CIF)

H3L2 (CIF)

H3L3 (CIF)

H3L4 (CIF)

■ AUTHOR INFORMATION

Corresponding Author

*E-mail: asaha@chemistry.jdvu.ac.in, amritasahachemju@gmail.com. Tel: +91-33-24572146.

ORCID

Amrita Saha: 0000-0001-9357-801X

Notes

The authors declare no competing financial interest.

DOI: 10.1021/acsomega.9b02181
ACS Omega 2020, 5, 145−157

■ ACKNOWLEDGMENTS

A.S. gratefully acknowledges the financial support of this work by the DST, India (Sanction No. SB/FT/CS-102/2014, dated Jully 18, 2015), and RUSA 2.0, Government of India (Sanction No. R-11/262/19, dated March 08, 2019).

■ REFERENCES

(1) Du, J.; Hu, M. M.; Fang, J. L.; Peng, X. J. Fluorescent chemodosimeters using "mild" chemical events for the detection of small anions and cations in biological and environmental media. *Chem. Soc. Rev.* **2012**, *41*, 4511−4535.

(2) Gonzáles, A. P. S.; Firmino, M. A.; Nomura, C. S.; Rocha, F. R. P.; Oliveira, P. V.; Gaubeur, I. Peat as a Natural Solid-phase for Copper Preconcentration and Determination in a Multicommuted Flow System Coupled to Flame Atomic Absorption Spectrometry. *Anal. Chim. Acta* **2009**, *636*, 198−204.

(3) Pathirathna, P.; Yang, Y. Y.; Forzley, K.; McElmurry, S. P.; Hashemi, P. Fast-scan Deposition-stripping Voltammetry at Carbon-fiber Microelectrodes: Real-time, Subsecond, Mercury Free Measurements of Copper. *Anal. Chem.* **2012**, *84*, 6298−6302.

(4) Becker, J. S.; Zoriy, M. V.; Pickhardt, C.; Palomero-Gallagher, N.; Zilles, K. Imaging of Copper, Zinc, and Other Elements in Thin Section of Human Brain Samples (Hippocampus) by Laser Ablation Inductively Coupled Plasma Mass Spectrometry. *Anal. Chem.* **2005**, *77*, 3208−3216.

(5) Liu, Y.; Liang, P.; Guo, L. Nanometer Titanium Dioxide Immobilized on Silica Gel as Sorbent for Preconcentration of Metal Ions Prior to their Determination by Inductively Coupled Plasma Atomic Emission Spectrometry. *Talanta* **2005**, *68*, 25−30.

(6) Zhou, Y.; Zhang, Y.; Yoon, J. F. Fluorescence and colorimetric chemosensors for fluoride-ion detection. *Chem. Rev.* **2014**, *114*, 5511−5571.

(7) Zhang, J. F.; Zhou, Y.; Yoon, J.; Kim, J. S. Recent progress in fluorescent and colorimetric chemosensors for detection of precious metal ions (silver, gold and platinum ions). *Chem. Soc. Rev.* **2011**, *40*, 3416−3429.

(8) Muller, G.; Bernuzzi, V.; Desor, D.; et al. Developmental alterations in offspring of female rats orally intoxicated by aluminum lactate at different gestation periods. *Teratology* **1990**, *42*, 253−261.

(9) Golub, M.; Donald, J. M.; et al. Effects of aluminum ingestion on spontaneous motor activity of mice. *Neurotoxicol. Teratol.* **1989**, *11*, 231−235.

(10) Williams, R. J. P. Recent aspects of aluminium chemistry and biology: a survey. *Coord. Chem. Rev.* **2002**, *228*, 93−97.

(11) Yokel, R. A. Aluminum chelation principles and recent advances. *Coord. Chem. Rev.* **2002**, *228*, 97−113.

(12) Baral, M.; Sahoo, S. K.; Kanungo, B. K. J. Tripodal amine catechol ligands: a fascinating class of chelators for aluminium(III). *J. Inorg. Biochem.* **2008**, *102*, 1581−1688.

(13) Kawahara, M.; Muramoto, K.; Kobayashi, K.; Mori, H.; Kroda, Y. Aluminum promotes the aggregation of Alzheimer's amyloid beta-protein in vitro. *Biochem. Biophys. Res. Commun.* **1994**, *198*, 531−535.

(14) Paik, S. R.; Lee, J. H.; Kim, D. H.; Chang, C. S.; Kim, J. Aluminum-induced structural alterations of the precursor of the non-A beta component of Alzheimer's disease amyloid. *Arch. Biochem. Biophys.* **1997**, *344*, 325−334.

(15) Lin, J. L.; Kou, M. T.; Leu, M. L. Effect of long-term low-dose aluminum-containing agents on hemoglobin synthesis in patients with chronic renal insufficiency. *Nephron* **1996**, *74*, 33−38.

(16) Good, P. F.; Olanow, C. W.; Perl, D. P. Neuromelanin-containing neurons of the substantia nigra accumulate iron and aluminum in Parkinson's disease: a LAMMA study. *Brain Res.* **1992**, *593*, 343−346.

(17) Darbre, P. D. Aluminium, antiperspirants and breast cancer. *J. Inorg. Biochem.* **2005**, *99*, 1912−1919.

(18) Singha, D. K.; Mahata, P. Highly selective and sensitive luminescenceturn-on-based sensing of Al^{3+} ions in aqueous medium using a MOF with freefunctional sites. *Inorg. Chem.* **2015**, *54*, 6373−6379.

(19) Diao, Q.; Ma, P.; Lv, L.; Li, T.; Sun, Y.; Wang, X.; Song, D. A water-soluble andreversible fluorescent probe for $Al^{3+}$and F^- in living cells. *Sens. Actuators, B* **2016**, *229*, 138−144.

(20) Naskar, B.; Modak, R.; Sikdar, Y.; Maiti, D. K.; Bauzá, A.; Frontera, A.; Katarkar, A.; Chaudhuri, K.; Goswami, S. Fluorescent sensing of $Al^{3+}$by benzophenone based Schiff base chemosensorand live cell imaging applications: impact of keto-enol tautomerism. *Sens. Actuators, B* **2017**, *239*, 1194−1204.

(21) Gupta, V. K.; Singh, A. K.; Kumawat, L. K. Thiazole Schiff base turn-on fluorescentchemosensor for Al^{3+} ion. *Sens. Actuators, B* **2014**, *195*, 98−108.

(22) Gupta, V. K.; Mergu, N.; Kumawat, L. K.; Singh, A. K. A reversible fluorescenceoff−on−off sensor for sequential detection of aluminum and acetate/fluorideions. *Talanta* **2015**, *144*, 80−89.

(23) Gupta, V. K.; Jain, A. K.; Maheshwari, G. Aluminum (III) selective potentiometricsensor based on morin in poly (vinyl chloride) matrix. *Talanta* **2007**, *72*, 1469−1473.

(24) Ding, Y.; Zhu, W.; Xu, Y.; Qian, X. A small molecular fluorescent sensor functionalized silica microsphere for detection and removal of mercury, cadmium, and lead ions in aqueous solutions. *Sens. Actuators, B* **2015**, *220*, 762−771.

(25) Wan, X.; Liu, T.; Liu, H.; Gu, L.; Yao, Y. Cascade OFF−ON−OFF fluorescent probe: dual detection of trivalent ions and phosphate ions. *RSC Adv.* **2014**, *4*, 29479−29484.

(26) Wang, L.; Li, H.; Cao, D. A new photoresponsive coumarin-derived Schiff base:chemosensor selectively for Al^{3+} and $Fe^{3+}$and fluorescence turn-on under room light. *Sens. Actuators, B* **2013**, *181*, 749−755.

(27) Lu, Y.; Huang, S.; Liu, Y.; He, S.; Zhao, L.; Zeng, X. Highly Selective and Sensitive Fluorescent Turn-on Chemosensor for Al^{3+} Based on a Novel Photoinduced Electron Transfer Approach. *Org. Lett.* **2011**, *13*, 5274−5277.

(28) (a) Tachapermpon, Y.; Thavornpradit, S.; Charoenpanich, A.; Sirirak, J.; Burgess, K.; Wanichacheva, N. Near-infrared aza-BODIPY fluorescent probe for selective Cu^{2+} detection and its potential in living cell imaging. *Dalton Trans.* **2017**, *46*, 16251−16256. (b) Liu, T.; Dong, Y.; Wan, X.; Li, W.; Yao, Y. An easy and accessible water-soluble sensor for the distinctive fluorescence detection of Zn^{2+} and Al^{3+} ions. *RSC Adv.* **2015**, *5*, 76939−76942.

(29) (a) Hou, L.; Feng, J.; Wang, Y.; Dong, C.; Shuang, S.; Wang, Y. Single fluorescein-based probe for selective colorimetric and fluorometric dual sensing of Al^{3+} and Cu^{2+}. *Sens. Actuators, B* **2017**, *247*, 451−460. (b) Qin, J.-C.; Fan, L.; Wang, B.-D.; Yang, Z.-Y.; Li, T.-R. The design of a simple fluorescent chemosensor for Al^{3+}/Zn^{2+} via two different approaches. *Anal. Methods.* **2015**, *7*, 716−722.

(30) Chen, X.; Pradhan, T.; Wang, F.; Kim, J. S.; Yoon, J. Fluorescent Chemosensors Based on Spiroring-Opening of Xanthenes and Related Derivatives. *Chem. Rev.* **2012**, *112*, 1910−1956.

(31) Kim, H. N.; Lee, M. H.; Kim, H. J.; Kim, J. S.; Yoon, J. A new trend in rhodamine-based chemosensors: application of spirolactam ring-opening to sensing ions. *Chem. Soc. Rev.* **2008**, *37*, 1465−1472.

(32) Dujols, V.; Ford, F.; Czarnik, A. W. A Long-Wavelength Fluorescent Chemodosimeter Selective for Cu(II) Ion in Water. *J. Am. Chem. Soc.* **1997**, *119*, 7386−7387.

(33) Quang, D. T.; Kim, J. S. Fluoro- and Chromogenic Chemodosimeters for Heavy Metal Ion Detection in Solution and Biospecimens. *Chem. Rev.* **2010**, *110*, 6280−6301.

(34) Li, X.-M.; Zhao, R.-R.; Yang, Y.; Lv, X. W.; Wei, Y.-L.; Tan, R.; Zhang, J.-F.; Zhou, Y. A Rhodamine-based fluorescent sensor for chromium ions and its application in bioimaging. *Chin. Chem. Lett.* **2017**, *28*, 1258−1261.

(35) Kwon, J. Y.; Jang, Y. J.; Lee, Y. J.; Kim, K. M.; Seo, M. S.; Nam, W.; Yoon, J. A Highly Selective Fluorescent Chemosensor for Pb^{2+}. *J. Am. Chem.* **2005**, *127*, 10107−10111.

(36) Wang, Y.; Chang, H.-Q.; Wu, W.-N.; Mao, X.-J.; Zhao, X.-L.; Yang, Y.; Xu, Z.-Q.; Xu, Z.-H.; Jia, L. A highly sensitive and selective colorimetric and off−on fluorescent chemosensor for Cu^{2+} based on

DOI: 10.1021/acsomega.9b02181
ACS Omega 2020, 5, 145−157

rhodamine 6G hydrazide bearing thiosemicarbazide moiety. *J. Photochem. Photobiol., A* **2017**, *335*, 10−16.
(37) Alam, R.; Bhowmick, R.; Islam, A. S. M.; katarkar, A.; Chaudhuri, K.; Ali, M. A rhodamine based fluorescent trivalent sensor (Fe^{3+}, Al^{3+}, Cr^{3+}) with potential applications for live cell imaging and combinational logic circuits and memory devices. *New J. Chem.* **2017**, *41*, 8359−8369.
(38) Jeong, J. W.; Rao, B. A.; Son, Y.-A. Rhodamine-chloronicotinaldehyde-based "OFF−ON" chemosensor for the colorimetric and fluorescent determination of Al^{3+} ions. *Sens. Actuators, B* **2015**, *208*, 75−84.
(39) Gupta, V. K.; Mergu, N.; Kumawat, L. K. Tunable photoluminescence of water-soluble AgInZnS−graphene oxide (GO) nanocomposites and their application in-vivo bioimaging. *Sens. Actuators, B* **2016**, *223*, 101−113.
(40) Ku, K.-S.; Muthukumar, P.; Angupillai, S.; Son, Y.-A. A new rhodamine 6 G based chemosensor for trace level Al^{3+} and its thin film application in 100% aqueous medium. *Sens. Actuators, B* **2016**, *236*, 184−191.
(41) Hou, L.; Feng, J.; Wang, Y.; Dong, C.; Shuang, S.; Wang, Y. Single fluorescein-based probe for selective colorimetric and fluorometric dual sensing of Al^{3+} and Cu^{2+}. *Sens. Actuators, B* **2017**, *247*, 451−460.
(42) Maniyazagan, M.; Mariadasse, R.; Nachiappan, M.; Jeyakanthan, J.; Lokanath, N. K.; Naveen, S.; Sivaraman, G.; Muthuraja, P.; Manisankar, P.; Stalin, T. Synthesis of rhodamine based organic nanorods for efficient chemosensor probe for Al (III) ions and its biological applications. *Sens. Actuators, B* **2018**, *254*, 795−804.
(43) Huang, Q.; Zhang, Q.; Wang, E.; Zhou, Y.; Qiao, H.; Pang, L.; Yu, F. A new "off-on" fluorescent probe for Al3+ in aqueous solution based on rhodamine B and its application to bioimaging. *Spectrochim. Acta, Part A.* **2016**, *152*, 70−76.
(44) (a) Yang, G.; Meng, X.; Fang, S.; Wang, L.; Wang, Z.; Wang, F.; Duan, H.; Hao, A. Two novel pyrazole-based chemosensors: 'naked-eye" colorimetric recognition of Ni^{2+} and Al^{3+} in alcohol and aqueous DMF media. *New J. Chem.* **2018**, *42*, 14630−14641. (b) Jeong, J. W.; Rao, B. A.; Son, Y. Rhodamine-chloronicotinaldehyde-based "OFF−ON" chemosensor for the colorimetric and fluorescent determination of Al^{3+} ions. *Sens. Actuators, B* **2015**, *208*, 75−84. (c) Chemate, S.; Sekar, N. A new rhodamine based OFF−ON fluorescent chemosensors forselective detection of Hg^{2+} and Al^{3+} in aqueous media. *Sens. Actuators, B* **2015**, *220*, 1196−1204. (d) Maity, S. B.; Bharadwaj, P. K. A Chemosensor Built with Rhodamine Derivatives Appended to an Aromatic Platform via 1,2,3-Triazoles: Dual Detection of Aluminum-(III) and Fluoride/Acetate Ions. *Inorg. Chem.* **2013**, *52*, 1161−1163. (e) Roy, A.; Shee, U.; Mukherjee, A.; Mandal, S. K.; Roy, P. Rhodamine-Based Dual Chemosensor for Al^{3+} and Zn^{2+} Ions with Distinctly Separated Excitation and Emission Wavelengths. *ACS Omega* **2019**, *4*, 6864−6875. (f) Ghosh, M.; Mandal, S.; Ta, S.; Das, D. Detection and discrimination of Al^{3+} and Hg^{2+} using a single probe:Nano-level determination, human breast cancer cell (MCF7) imaging, binary logic gate development and sea fish sample analysis. *Sens. Actuators, B* **2017**, *249*, 339−347. (g) Alam, R.; Bhowmick, R.; Islam, A. S. M.; katarkar, A.; Chaudhuri, K.; Ali, M. A rhodamine based fluorescent trivalent sensor (Fe^{3+}, Al^{3+}, Cr^{3+}) with potential applications for live cell imaging and combinational logic circuits and memory devices. *New J. Chem.* **2017**, *41*, 8359−8369. (h) Fu, Y.; Jiang, X.-J.; Zhu, Y.-Y.; Zhou, B.-J.; Zang, S.-Q.; Tang, M.-S.; Zhang, H.-Y.; Maka, T. C. W. A new fluorescent probe for Al^{3+} based on rhodamine 6G and its application to bioimaging. *Dalton Trans.* **2014**, *43*, 12624−12632. (i) Sahana, A.; Banerjee, A.; Lohar, S.; Banik, A.; Mukhopadhyay, S. K.; Safin, D. A.; Babashkina, M. G.; Bolte, M.; Garcia, Y.; Das, D. FRET based tri-color emissive rhodamine−pyrene conjugate as an Al^{3+} selective colorimetric and fluorescence sensor for living cell imaging. *Dalton Trans.* **2013**, *42*, 13311−13314. (j) Roy, A.; Mukherjee, R.; Dam, B.; Dam, S.; Roy, P. A rhodamine-based fluorescent chemosensor for Al^{3+}: is it possible to control the metal ion selectivity of a rhodamine-6G based chemosensor. *New J. Chem.* **2018**, *42*, 8415−8425. (k) Sen, B.; Mukherjee, M.; Banerjee, S.; Pal, S.; Chattopadhyay, P. A rhodamine-based 'turn-on' Al^{3+} ion-selective reporter and the resultant complex as a secondary sensor for F^- ion are applicable to living cell staining. *Dalton Trans.* **2015**, *44*, 8708−8717. (l) Sahana, A.; Banerjee, A.; Lohar, S.; Sarkar, B.; Mukhopadhyay, S. K.; Das, D. Rhodamine-Based Fluorescent Probe for Al^{3+} through Time-Dependent PET−CHEF−FRET Processes and Its Cell Staining Application. *Inorg. Chem.* **2013**, *52*, 3627−3633.
(45) Yang, X. F.; Guo, X. Q.; Zhao, Y. B. Development of a novel rhodamine-type fluorescent probe to determine peroxynitrite. *Talanta* **2002**, *57*, 883−890.
(46) Benesi, H. A.; Hildebrand, J. H. A Spectrophotometric Investigation of the Interaction of Iodine with Aromatic Hydrocarbons. *J. Am. Chem. Soc.* **1949**, *71*, 2703−2707.
(47) Pradhan, A. B.; Mandal, S. K.; Banerjee, S.; Mukherjee, A.; Das, S.; Bukhsh, A. R. K.; Saha, A. A highly selective fluorescent sensor for zinc ion based on quinoline platform with potential applications for cell imaging studies. *Polyhedron* **2015**, *94*, 75−82.
(48) Sheldrick, G. M. *SAINT, version 6.02, SADABS, version 2.03*; Bruker AXS Inc.: Madison, Wisconsin, 2002.
(49) Sheldrick, G. M. *SADABS: Software for Empirical Absorption Correction*; University of Gottingen, Institute fur Anorganische Chemieder Universitat: Gottingen, Germany, 1999−2003.
(50) Sheldrick, G. M. Crystal structure refinement with SHELXL. *Acta Cryst.* **2015**, *C71*, 3−8.
(51) Frisch, M. J.; Trucks, G. W.; Schlegel, H. B.; Scuseria, G. E.; Robb, M. A.; Cheeseman, J. R.; Scalmani, G.; Barone, V.; Mennucci, B.; Petersson, G. A.; Nakatsuji, H.; Caricato, M.; Li, X.; Hratchian, H. P.; Izmaylov, A. F.; Bloino, J.; Zheng, G.; Sonnenberg, J. L.; Hada, M.; Ehara, M.; Toyota, K.; Fukuda, R.; Hasegawa, J.; Ishida, M.; Nakajima, T.; Honda, Y.; Kitao, O.; Nakai, H.; Vreven, T.; Montgomery, J. A., Jr.; Peralta, J. E.; Ogliaro, F.; Bearpark, M.; Heyd, J.; Brothers, J. E.; Kudin, K. N.; Staroverov, V. N.; Kobayashi, R.; Normand, J.; Raghavachari, K.; Rendell, A.; Burant, J. C.; Iyengar, S. S.; Tomasi, J.; Cossi, M.; Rega, N.; Millam, J. M.; Klene, M.; Knox, J. E.; Cross, J. B.; Bakken, V.; Adamo, C.; Jaramillo, J.; Gomperts, R.; Stratmann, R. E.; Yazyev, O.; Austin, A. J.; Cammi, R.; Pomelli, C.; Ochterski, J. W.; Martin, R. L.; Morokuma, K.; Zakrzewski, V. G.; Voth, G. A.; Salvador, P.; Dannenberg, J. J.; Dapprich, S.; Daniels, A. D.; Farkas, Ö.; Foresman, J. B.; Ortiz, J. V.; Cioslowski, J.; Fox, D. J. *Gaussian 09*, revision D.01; Gaussian Inc.: Wallingford, CT, 2009.
(52) Becke, A. D. Density-functional thermochemistry. III. The role of exact exchange. *J. Chem. Phys.* **1993**, *98*, 5648−5652.
(53) Lee, C.; Yang, W.; Parr, R. G. Development of the Colle-Salvetti correlation-energy formula into a functional of the electron density. *Phys. Rev. B* **1988**, *37*, 785−789.
(54) Hay, P. J.; Wadt, W. R. Ab initio effective core potentials for molecular calculations. Potentials for K to Au including the outermost core orbitals. *J. Chem. Phys.* **1985**, *82*, 270−283.
(55) Wadt, W. R.; Hay, P. Ab initio effective core potentials for molecular calculations. Potentials for main group elements Na to Bi. *J. Chem. Phys.* **1985**, *82*, 284−298.
(56) Hay, P. J.; Wadt, W. R. Ab initio effective core potentials for molecular calculations. Potentials for K to Au including the outermost core orbitals. *J. Chem. Phys.* **1985**, *82*, 299−310.
(57) Petersson, G. A.; Bennett, A.; Tensfeldt, T. G.; Al-Laham, M. A.; Shirley, W. A.; Mantzaris, J. A complete basis set model chemistry. I. The total energies of closed-shell atoms and hydrides of the first-row elements. *J. Chem. Phys.* **1988**, *89*, 2193−2218.
(58) Petersson, G. A.; Al-Laham, M. A. A complete basis set model chemistry. II. Open-shell systems and the total energies of the first-row atoms. *J. Chem. Phys.* **1991**, *94*, 6081−6090.
(59) Bauernschmitt, R.; Ahlrichs, R. Treatment of electronic excitations within the adiabatic approximation of time dependent density functional theory. *Chem. Phys. Lett.* **1996**, *256*, 454−464.
(60) Stratmann, R. E.; Scuseria, G. E.; Frisch, M. An efficient implementation of time-dependent density-functional theory for the calculation of excitation energies of large molecules. *J. Chem. Phys.* **1998**, *109*, 8218−8224.

DOI: 10.1021/acsomega.9b02181
ACS Omega 2020, 5, 145−157

(61) Casida, M. E.; Jamorski, C.; Casidaand, K. C.; Salahub, D. R. Density- and density-matrix-based coupled Kohn−Sham methods for dynamic polarizabilities and excitation energies of molecules. *J. Chem. Phys.* **1998**, *108*, 4439−4449.
(62) Barone, V.; Cossi, M. Quantum Calculation of Molecular Energies and Energy Gradients in Solution by a Conductor Solvent Model. *J. Phys. Chem. A* **1998**, *102*, 1995−2001.
(63) Cossi, M.; Barone, V. Time-dependent density functional theory for molecules in liquid solutions. *J. Chem. Phys.* **2001**, *115*, 4708−4717.
(64) Cossi, M.; Rega, N.; Scalmani, G.; Barone, V. Energies, structures, and electronic properties of molecules in solution with the C-PCM solvation model. *J. Comput. Chem.* **2003**, *24*, 669−681.
(65) O'Boyle, N. M.; Tenderholt, A. L.; Langner, K. M. cclib: a library for package-independent computational chemistry algorithms. *J. Comput. Chem.* **2008**, *29*, 839−845.

DOI: 10.1021/acsomega.9b02181
ACS Omega 2020, 5, 145−157